

Laboratory Simulation of Arched Magnetic Flux Rope Eruptions in the Solar Atmosphere

S. K. P. Tripathi* and W. Gekelman†

Physics and Astronomy, University of California at Los Angeles, Los Angeles, California 90095, USA
(Received 9 February 2010; published 13 August 2010)

Dramatic eruption of an arched magnetic flux rope in a large ambient plasma has been studied in a laboratory experiment that simulates coronal loops. The eruption is initiated by laser generated plasma flows from the footpoints of the rope that significantly modify the magnetic-field topology and link the magnetic-field lines of the rope with the ambient plasma. Following this event, the flux rope erupts by releasing its plasma into the background. The resulting impulse excites intense magnetosonic waves that transfer energy to the ambient plasma and subsequently decay.

DOI: 10.1103/PhysRevLett.105.075005

PACS numbers: 52.72.+v, 52.38.Mf, 96.60.pf

Coronal loops, prominences, and filaments are arched magnetic flux rope (AMFR) structures in the solar atmosphere that confine plasma, remain stable for minutes to days, and suddenly erupt—leading to the onset of energetic events such as jets, transients, flares, and coronal mass ejections [1–4]. Solar AMFRs have their footpoints rooted underneath the photosphere with a leading edge extending up to coronal heights; thus, they can efficiently transport energy and plasma from the solar surface to its outer atmosphere. The exact relationship between various AMFR instabilities and solar energetic phenomena is an active area of research encompassing outstanding problems in solar physics [5–9].

Laboratory experiments have started playing important roles in exploring the solar AMFR dynamics [10]. A few examples of such experiments are laboratory studies of two interacting magnetic flux ropes [11–13], the effect of a strapping magnetic field on the AMFR expansion [14], and production of kinetic plasma jets from AMFRs [15]. Magnetized arc plasma sources have been used in conventional laboratory experiments that produced AMFRs that evolve in vacuum and carry several kiloampere current [12]. These AMFRs are observed to undergo severe current-driven (e.g., kink) instabilities immediately after the plasma breakdown. Traditional astronomical [16] and spacecraft observations, however, ubiquitously show solar AMFRs with stable appearances suspended for longer duration (many Alfvén transit times, i.e., the time for Alfvén wave to travel from one footpoint to the other) followed by their sudden eruption [9,13,17]. These observations suggest that the internal current of stable AMFRs is well below the current required for the kink instability and a source of instability (e.g., magnetic flux and hot plasma injection from footpoints [18], changes in surroundings such as photospheric flows and overlying fields [19]) appears at a later time to drive the eruption. Laboratory simulation of this complex eruption dynamics requires a nonconventional approach where stable AMFRs could be produced and a subsequent source of instability could be applied to trigger their eruption. We report results from a laboratory experiment which possesses unprecedented ca-

pability of simulating the impulsive eruption of a stable AMFR and diagnosing it with high spatiotemporal resolutions. Three properly synchronized plasma sources are operated with a high-repetition rate to produce the AMFR in an ambient magnetized plasma. After brief description of the experimental setup, initial results on the AMFR eruption and excitation of magnetosonic waves will be presented.

The experiment is performed in a cylindrical vacuum chamber (4.0 m long, 1.0 m diameter) at 5.0×10^{-4} torr argon gas pressure and 2.5 mT axial magnetic field. A rectangular LaB₆ cathode (0.2 m × 0.2 m, $T = 1700$ °C) and a wire-mesh anode (0.27 m from the cathode) are mounted at one end of the chamber to produce an ambient plasma ($n = 2.0 \times 10^{18}$ m⁻³, $T_e \sim 4.0$ eV, pulse width $\tau_L = 20$ ms, repetition rate $\tau_{\text{rep}} = 0.5$ Hz). The AMFR is produced with an additional plasma source. As shown in Fig. 1(a), the AMFR plasma source consists of an annular copper anode and an annular LaB₆ cathode ($T = 1825$ °C) mounted on two radially movable shafts that make equal angles from the $y = 0$ symmetry plane. The AMFR footpoints (anchored on the electrodes) are separated by 23 cm. Each AMFR electrode [outer (inner) diameter: 7.6 cm (1.3 cm)] is surrounded by an electromagnet to produce an arched vacuum magnetic field with 0.1 T strength at the footpoints. In this setup, magnetic-field lines of the AMFR make a 90° angle from the magnetic-field lines of the ambient plasma [see Fig. 1(a)]. A capacitor bank charged at 155 V produces the AMFR plasma ($n \sim 10^{19}$ m⁻³, $T_e = 10$ eV, current $I = 42$ A, $\tau_L = 1.0$ ms, $\tau_{\text{rep}} = 0.5$ Hz) in the afterglow of the ambient plasma. A stable AMFR, characterized by a stationary density profile and a persistent camera image, is produced in 150 μ s after application of the voltage on the electrodes.

Eruption of the stable AMFR is initiated by firing two identical laser beams ($\lambda = 1064$ nm, $\tau_L = 8$ –12 ns, $E_b \sim 0.8$ J/pulse for each beam) at $t = 0$ μ s that strike carbon target rods placed behind holes in the AMFR electrodes. The laser ablates the targets and generates carbon plasma jets from both footpoints. Each target rod is moved in small

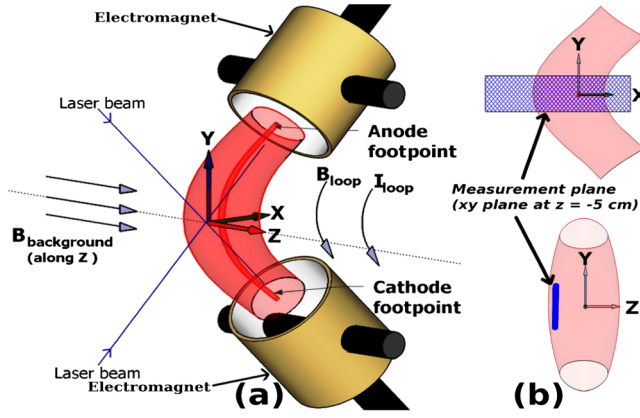


FIG. 1 (color online). (a) Schematic of the experiment showing the AMFR, laser beams, vacuum magnetic fields, and xyz coordinate system. The origin of the coordinate system is located on the machine axis (dotted line) where both laser beams intersect. The AMFR moves through the origin as it evolves. (b) Side (xy) and front (yz) views of the rectangular measurement plane and AMFR [shaded (pink) region].

azimuthal and axial steps by computer controlled stepper motors to provide a fresh target surface at every shot. This is critical for maintaining the good reproducibility ($\delta n/n$, $\delta B/B < 0.005$) and high-repetition rate of the experiment. The control system also moves diagnostic probes in the xy plane using a 2D probe drive system that can be mounted at various z locations on the vacuum chamber. Single Langmuir and air-cooled magnetic loop (B -dot) probes are the main diagnostic tools. The measurement plane [shown in Fig. 1(b)] is chosen at $z = -5$ cm to make sure that probes are not destroyed by laser beams in the $z = 0$ cm plane.

The magnetic-field line twist in an AMFR is given by a useful parameter $\Phi(r) = (LB_\theta)/(rB_\zeta)$. Here, L , r , θ , and ζ are length of the AMFR, radial distance from the AMFR axis, angle around the AMFR axis measured from the positive x axis, and distance from the cathode measured along the curved axis of the AMFR, respectively. The arched vacuum magnetic field primarily corresponds to B_ζ . At the edge ($r = b$) of the AMFR, $\Phi(b) = (\mu_0 LI)/(2\pi b^2 B_{\zeta b})$. In this order of magnitude analysis, $\Phi(b)$ represents an average twist over θ for fixed r and ζ . The actual AMFR would have larger twist in the inboard region ($\theta = 3\pi/2 - \pi/2$) compared to the outboard region ($\theta = \pi/2 - 3\pi/2$). A MHD stability analysis by Hood and Priest [20] for a straight magnetic flux tube with anchored ends predicts kink instability when $\Phi > \Phi_{\text{crit}} \approx 2\pi - 6\pi$. In the absence of the laser-plasma jets, $I = 42$ A is enclosed in the $r < b = 3.81$ cm region of the AMFR ($L \sim 0.5$ m) near its footpoints ($B_{\zeta b} \sim 0.1$ T) which gives $\Phi(b) \sim 0.03$ [at the AMFR apex $\Phi(b) \sim 0.08$]. This calculation shows that in the absence of the laser plasma, $\Phi(b)$ is too small and hence the AMFR is stable. In the presence of the laser-plasma jets, a 800 A current spike is recorded in a narrow region ($b \sim 0.5$ cm) near the footpoints where $\Phi(b) \sim$

32.6. Thus, a significant increase in $\Phi(b)$ is observed near the footpoints following the injection of the plasma jets. This mimics the initiation of the instability by magnetic flux injection suggested in Refs. [4,18]. Direct measurement of the B fields reveals even larger twist in the apex region [$\Phi(r = 5$ cm, $\theta = 3\pi/2$, $\zeta = L/2) \sim 82$] at $t = 1.0$ μs . This analysis demonstrates that the initial stable AMFR becomes extremely kink unstable following the injection of the plasma jets. An order of magnitude increase in the discharge current following the laser trigger significantly increases the outward hoop force leading to the force imbalance and an outward motion of the AMFR. The experimental results in the following paragraphs present the essential features of this outward-expanding kink-unstable AMFR.

Figure 2(a) is an image of a stable argon AMFR recorded at $t = 0.24$ μs (kink unstable after $t \sim 0.5$ μs) using a CCD camera with a 0.10 μs exposure time. The ambient plasma was turned off to obtain a clear image of the AMFR. This image also shows two plasma jets emanating from the AMFR footpoints. By comparing an unfiltered image with a 460 nm passband filtered image, it was confirmed that the jets are primarily composed of C^{++} ions. The time-of-flight measurements from similar camera images reveal that both plasma jets propagate with $\sim 5.0 \times 10^4$ m/s supersonic velocity (ion acoustic velocity c_s in the AMFR $\sim 5.0 \times 10^3$ m/s). In the AMFR, the Alfvén velocity v_A near the footpoints is $\sim 10^5$ m/s and in the apex region it is $\sim 10^4$ m/s. Hence, the plasma jets are sub-Alfvénic near the footpoints. The plasma β (ratio of plasma pressure and magnetic-field pressure) is $\sim 10^{-3}$ for the argon plasma in the stable AMFR near its footpoints. The Lundquist number ($\mu_0 L v_A / \eta$, where η is Spitzer resistivity) is $10^3 - 10^4$ and the ratio of the AMFR radius to the argon ion gyroradius is ~ 12 .

Evolution of the AMFR density profile during its eruption is shown at six distinct times in Fig. 2(b). In the absence of the laser plasma, the density profile of the stable

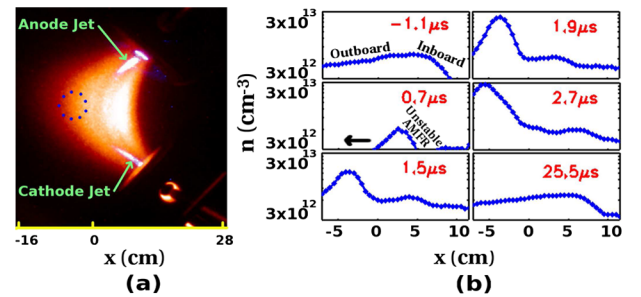


FIG. 2 (color online). (a) Image of a stable AMFR. Laser generated plasma jets are shown by arrows and the approximate location of the linkage region is indicated by the dots. (b) Time evolution of the plasma density profile of the AMFR during the eruption is shown at $y = 0$ cm in the xy measurement plane of Fig. 1(b). The outward motion (along $-x$ direction of the arrow) of the erupting AMFR is a prominent feature that can be observed in these line plots.

AMFR remains nearly stationary after initial $150 \mu\text{s}$ of its formation. The laser beams are triggered $450 \mu\text{s}$ later at $t = 0 \mu\text{s}$; thus, the ratio of the stable AMFR duration to the Alfvén transit time ($\sim 9 \mu\text{s}$) is 50. The $t = -1.1 \mu\text{s}$ plot shows the density profile during this stable phase. Following the laser trigger, the plasma is released from the edge of the stable AMFR and a much thinner and dynamic AMFR with a clearly identifiable density peak emerges in the $t = 0.7 \mu\text{s}$ plot. Note that this density profile is measured at $r = 5 \text{ cm}$ and the actual density on the AMFR axis could be much higher. As discussed earlier, this thin and dynamic AMFR is expected to move in the outward direction along the $-x$ direction. This outward motion is seen in the $t = 0.7\text{--}2.7 \mu\text{s}$ plots. The higher expansion velocity during earlier times ($0.7\text{--}1.5 \mu\text{s}$, $v \sim 8.4 \times 10^4 \text{ m/s}$) compared to the later times ($1.9\text{--}2.7 \mu\text{s}$, $v \sim 3.1 \times 10^4 \text{ m/s}$) shows the gradual decay of the impulsive (large burst of activity after quiescent stage) phase of the AMFR eruption. The outward moving plasma is ultimately absorbed into the background and a new AMFR forms since the discharge power supply is kept on during $t = -600\text{--}400 \mu\text{s}$. The density profile of the reforming AMFR at $t = 25.5 \mu\text{s}$ closely resembles the initial density profile of the stable AMFR.

The strength of the AMFR magnetic field is weakest in its apex region. If we superimpose the large scale magnetic field of the ambient plasma over the closed magnetic field of the AMFR [see Fig. 1(a)], it can be seen that the AMFR magnetic-field lines emerge out from its outboard-apex region and link with the magnetic-field lines of the ambient plasma. We call this outboard-apex region of the AMFR the “linkage region” and its approximate location for a stable AMFR is marked in Fig. 2(a). The linkage region for an unstable AMFR is expected to move in the outboard direction. In the linkage region, the plasma β is locally large (~ 1) and magnetic-field lines of the ambient plasma enter into the AMFR. In the absence of the laser beams and ambient plasma, continuous leakage of the AMFR plasma originating from its linkage region can be easily seen with the naked eye.

The surface plot of $n(x, t)$ has been displayed in Fig. 3 to show the intense density wave ($\partial n/n \sim 16\%$, $\partial B/B \sim 20\%$) that appears immediately after the AMFR eruption. This wave is easily identified in the xt plots as there is single dominant frequency and wavelength. The eruption phase [discussed earlier in reference to Fig. 2(b)] is compressed on the much larger time scale in Fig. 3. Following the eruption, the AMFR expands away from the x range in Fig. 3 and the post-eruption data characterize the ambient plasma that is left behind and the new AMFR which slowly forms. The phase fronts of the wave are more clearly seen in the inset of Fig. 3. The V shape of the phase fronts in the inset evince that the wave propagates radially away from the source region. In the edge of the plasma ($|x| > 5 \text{ cm}$), the phase fronts are nearly vertical, indicating a density oscillation and not a wave. The large density perturbation and wave propagation perpendicular to the equilibrium

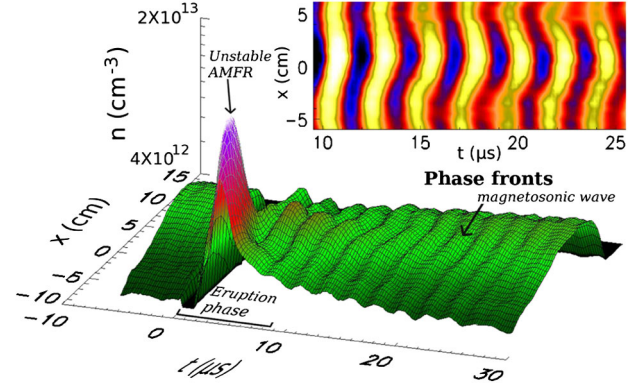


FIG. 3 (color online). Surface plot $n(x, t)$ covering the eruption and magnetosonic wave propagation time phases of the AMFR. The V-shaped phase fronts of the magnetosonic wave are better visualized in the inset. The light (yellow) and dark (blue) regions show the crest and trough of the wave, respectively.

magnetic field are important characteristics of a magnetosonic wave. Moreover, the wave is excited at frequency f such that $f_{ci} \ll f < f_{lh}$, where f_{ci} and f_{lh} are ion cyclotron and lower hybrid frequencies, respectively. This is above the frequency range where shear Alfvén waves propagate. The phase velocity of a fast magnetosonic wave propagating normal to the magnetic field, in a plasma with $v_A \gg c_s$, is nearly equal to v_A [21]. Near the source region of the wave, average values of $n \sim 2.0 \times 10^{18} \text{ m}^{-3}$ and $B \sim 12.2 \text{ mT}$ give $v_A = 3.0 \times 10^4 \text{ m/s}$. The frequency of the observed oscillation is 417 kHz and the associated wavelength (in the xy plane) is $8.5 \pm 0.5 \text{ cm}$. Therefore, the observed phase velocity, $v_\phi = f\lambda = 3.6 \times 10^4 \text{ m/s}$, is close to the calculated phase velocity of the magnetosonic wave. The magnetosonic wave decays in $30 \mu\text{s}$ followed by noticeable change in the density, plasma potential, and electron temperature of the ambient plasma.

The 2D magnetic-field vectors of the erupting AMFR are displayed at four distinct times in Fig. 4(a). Observation of an azimuthal magnetic field in all frames of Fig. 4(a) reveals the presence of an axial current at $z = -5 \text{ cm}$. An azimuthal magnetic-field pattern is also recorded in a second xy plane at $z = -64 \text{ cm}$ which manifests the presence of an axial current channel linking the AMFR and the ambient plasma. The current channel emerges from the linkage region and initially propagates along the x direction (see the x motion in 1.0 and $1.5 \mu\text{s}$ frames). Following the eruption ($t > 8 \mu\text{s}$), the current channel emerges from a stationary location in the xy plane, oscillates with the magnetosonic wave frequency, and decays after $30 \mu\text{s}$ in accordance with the density measurements. The 3D magnetic-field vectors, shown in Fig. 4(b), indicate that B_z (sticking out of the xy plane) is a dominant magnetic-field component. Note that B_z is positive in the inboard region and negative in the outboard region. This is consistent with the generation of an azimuthal magnetic field by the AMFR current. The magnitude of B_z is higher in the inboard region due to the asymmetry

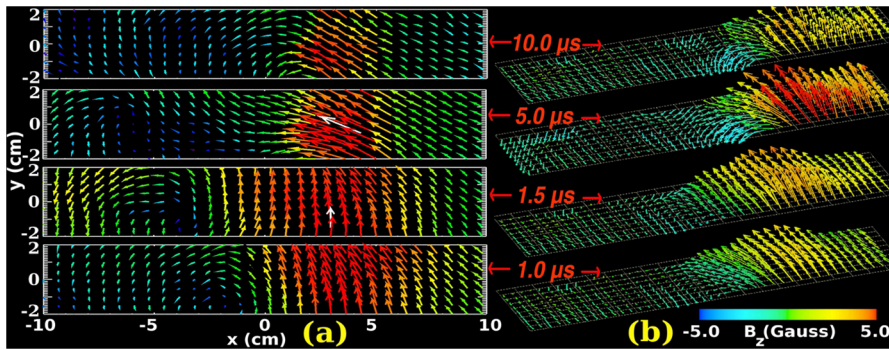


FIG. 4 (color online). Time evolution of the magnetic-field vectors of the AMFR displayed in the measurement plane of Fig. 1(b) at $z = -5$ cm after the laser trigger at $t = 0$ μ s. Panel (a) shows 2D projection of the AMFR magnetic field. The B_z component is suppressed. Panel (b) shows 3D magnetic field in a perspective view of the measurement plane.

in the magnetic field of the AMFR. At later times ($t > 10$ μ s, data not shown), the net $|B|$ shows maxima and minima in the xy plane similar to the maxima and minima generated by the density wave in Fig. 3.

The experimental results establish that the injection of plasma flow and associated current triggers the eruption of a stable AMFR which in turn excites the fast magnetosonic wave and plasma oscillations. It was shown that the fast wave exists only when the flows are present. Several theoretical models rely on the existence of flows, waves, and oscillations to explain aspects of the solar AMFRs [22] and heating of the corona [6–8]. Most of these models remain speculative because of the poor spatiotemporal resolutions in the solar observations and lack of direct measurement of the coronal magnetic field. Preliminary results presented in this Letter show that the laboratory AMFR exhibits important characteristics of an erupting solar AMFR. Our measurements have identified critical changes associated with the eruption, namely, the outward expansion of the AMFR, development of a large twist in its magnetic field, release of the AMFR plasma, and excitation of the fast wave. Observation of the fast wave is particularly important since fast waves can transport energy across magnetic-field lines (unlike shear Alfvén waves), efficiently carry energy flux (group velocity $\sim v_A$), and exist at frequencies higher than the cyclotron frequency [21]. These unique features make the fast wave a potential candidate for coronal heating. Recent spacecraft observations have also revealed that flows and intense magnetosonic waves coexist in the solar AMFRs. Such magnetosonic waves are estimated to contain sufficient energy to heat the AMFR to the coronal temperatures [23–25].

In our experiment, relative magnitudes of the plasma parameters of the AMFR and the ambient plasma were chosen by careful scaling of the solar plasma parameters. The AMFR eruption occurs on a time scale faster than the Spitzer resistive time (~ 200 μ s), making it relevant to the solar eruptions. Detailed 3D measurements are planned to study the structure of the post-eruption laboratory AMFRs and examine their scaling property with respect to their coronal-mass-ejection-like solar counterparts.

The authors acknowledge valuable contributions in the design of the experiment from A. Collette, P. Prybil, C. Cooper, Z. Lucky, and M. Drandell and thank J. Chen

(NRL) for his helpful suggestions. The research was performed at the Basic Plasma Science Facility, UCLA, which is jointly funded by NSF and DOE.

*tripathi@physics.ucla.edu

†gekelman@physics.ucla.edu

- [1] K. R. Lang, *The Cambridge Encyclopedia of the Sun* (Cambridge University Press, Cambridge, England, 2001), 1st ed., pp. 106–143.
- [2] E. Hildner *et al.*, *Sol. Phys.* **42**, 163 (1975).
- [3] H. Cremades and V. Bothmer, *Astron. Astrophys.* **422**, 307 (2004).
- [4] J. Chen, *J. Geophys. Res.* **101**, 27 499 (1996).
- [5] Y. Fan and S. E. Gibson, *Astrophys. J.* **668**, 1232 (2007).
- [6] M. J. Aschwanden, *Astrophys. J.* **560**, 1035 (2001).
- [7] K. J. H. Phillips, *Plasma Phys. Controlled Fusion* **42**, 113 (2000).
- [8] C. Jordan, *Plasma Phys. Controlled Fusion* **42**, 415 (2000).
- [9] B. R. Dennis and R. A. Schwartz, *Sol. Phys.* **121**, 75 (1989).
- [10] D. Alexander, *Astrophys. Space Sci.* **307**, 197 (2007).
- [11] E. E. Lawrence and W. Gekelman, *Phys. Rev. Lett.* **103**, 105002 (2009).
- [12] J. F. Hansen, S. K. P. Tripathi, and P. M. Bellan, *Phys. Plasmas* **11**, 3177 (2004).
- [13] T. P. Intrator, X. Sun, G. Lapenta, L. Dorf, and I. Furno, *Nature Phys.* **5**, 521 (2009).
- [14] J. F. Hansen and P. M. Bellan, *Astrophys. J.* **563**, L183 (2001).
- [15] S. K. P. Tripathi, P. M. Bellan, and G. S. Yun, *Phys. Rev. Lett.* **98**, 135002 (2007).
- [16] C. G. Abbot, *The Sun* (D. Appleton and Company, New York, 1911), pp. 128–182.
- [17] P. Romano *et al.*, *Astron. Astrophys.* **498**, 901 (2009).
- [18] J. Krall, J. Chen, and R. Santoro, *Astrophys. J.* **539**, 964 (2000).
- [19] S. K. Antiochos, *Astrophys. J.* **502**, L181 (1998).
- [20] A. W. Hood and E. R. Priest, *Sol. Phys.* **64**, 303 (1979).
- [21] S. R. Habbal, E. Leer, and T. E. Holzer, *Sol. Phys.* **64**, 287 (1979).
- [22] J. Chen and P. W. Schuck, *Sol. Phys.* **246**, 145 (2007).
- [23] L. Ofman and T. J. Wang, *Astron. Astrophys.* **482**, L9 (2008).
- [24] V. M. Nakariakov *et al.*, *Science* **285**, 862 (1999).
- [25] B. Roberts, *Sol. Phys.* **193**, 139 (2000).